# Single-step Flame Aerosol Synthesis of Active and Stable Nanocatalysts for the Dry Reforming of Methane

Mohammad Moein Mohammadi, Chintan Shah, Sandeep Kumar Dhandapani, Junjie Chen, Shema Rachel Abraham, William Sullivan, Raymond D. Buchner, Eleni A. Kyriakidou, Haiqing Lin, Carl R. F. Lund, Mark T. Swihart*

*Department of Chemical and Biological Engineering, University at Buffalo, The State University of New York, Buffalo, NY 14260, USA*

*swihart@buffalo.edu

## ABSTRACT

We introduce a flame-based aerosol process for producing supported non-noble metal nanocatalysts from inexpensive aqueous metal salt solutions, using catalysts for dry reforming of methane (DRM) as a prototype. Flame-synthesized nickel-doped magnesia (MgO) nanocatalyst (NiMgO-F) was fully physico-chemically characterized, and tested in a flow reactor system, where it showed stable DRM activity from 500°C to 800°C. A kinetic study was conducted and apparent activation energies were extracted for the temperature range of 500-650°C. It was then compared with Ni-decorated MgO nanopowder prepared by wet impregnation of 1) flame-synthesized MgO (NiMgO-FI); and 2) commercial MgO nanopowder (NiMgO-CI), and with 3) NiMgO catalyst prepared by co-precipitation (NiMgO-CP). NiMgO-F showed the highest catalytic activity per mass and per metallic surface area and was stable for continuous $H_2$ production at 700°C for 50 h. Incorporation of potential promoters and co-catalysts was also demonstrated, but none showed significant performance improvement. More broadly, nanomaterials produced by this approach could be used as binary or multicomponent catalysts for numerous catalytic processes.

**Keywords:** Dry reforming, Methane, $CO_2$ utilization, Flame aerosol synthesis, Nickel

## INTRODUCTION

Dry reforming of methane (DRM) converts methane and carbon dioxide, two major greenhouse gases, to an equimolar mixture of hydrogen and carbon monoxide, *i.e.,* syngas, **Equation (1)**. Compared to the other reforming reactions such as steam reforming or partial oxidation, DRM produces a lower $H_2$ to CO ratio that is suitable for the production of liquid fuels *via* the Fischer-Tropsch process.[1] Although this process has great potential for simultaneous $CO_2$ utilization and syngas production, it is not considered an industrially viable or mature technology. Challenges include undesirable side reactions such as the reverse water gas shift reaction, **Equation (2)**, which consumes part of the produced $H_2$ and produces unwanted water, and the Boudouard reaction, **Equation (3)**, and methane cracking, which deactivate the catalyst by carbon deposition, *i.e.*, coking.[2] While methane cracking is formally the sum of **Equation (1)** and **Equation (2)**, and not independent from a thermodynamic perspective, kinetically it is a distinct pathway to carbon deposition. Hence, the synthesis of highly active and stable DRM catalysts remains an important topic of investigation that continues to attract the attention of researchers.[3]

$$CH_4 + CO_2 \leftrightarrows 2\,CO + 2\,H_2 \qquad (1)$$

$$CO_2 + H_2 \leftrightarrows CO + H_2O \qquad (2)$$

$$2\,CO \rightarrow C + CO_2 \qquad (3)$$

Supported catalysts using noble metals such as rhodium (Rh),[4] ruthenium (Ru),[5] and platinum (Pt),[6] exhibit high activity and are relatively resistant to coking. However, the

high cost and limited availability of such metals constrain their use in the DRM process.[7] Thus, lower cost catalysts based on non-noble metals such as nickel (Ni) could improve the economics and practicality of this process.[8] Performance of supported Ni catalysts can be comparable to that of noble metal-based catalysts due to their ability to activate C-H bonds of methane, which is generally believed to be the rate-determining step in the DRM reaction.[9]

One approach to address the drawbacks of Ni-based catalysts (mostly deactivation *via* coke formation), is selection of an appropriate support. The mechanism of the DRM process is strongly dependent on metal-support interactions.[10] For instance, silica ($SiO_2$)-based catalysts follow a mono-functional pathway (activation of both reactants by the metal),[11] while non-inert supports follow a bi-functional mechanism (activation of $CH_4$ on the metal and activation of $CO_2$ by the support).[12] Lewis base metal oxides promote the adsorption of acidic $CO_2$ and hinder coke formation through the reaction between $CO_2$ and the carbon produced by $CH_4$ decomposition.[13]

Another approach to limit the disadvantages of Ni-based catalysts involves using Ni particles with a small diameter. Ni nanoparticles with dimensions below a critical diameter (< 9 nm) and narrow size distribution have been shown to exhibit higher resistance to deactivation in the DRM process than larger, more polydisperse particles.[14] In another study, Ni nanoparticles with a diameter of 2.6 nm showed 4.1 times higher $CH_4$ turnover frequency than those with a diameter of 17.3 nm.[15] The two approaches, incorporation of an appropriate support and small Ni particle size, are linked and depend strongly upon the preparation method and the catalyst synthesis parameters.[16]

Among the potential supports, MgO has been widely reported as being effective because of its high thermal stability, low cost, and unique ability to form a solid solution with NiO.[17-18] MgO has the same crystal structure as NiO, and $Mg^{2+}$ has almost the same ionic radius as $Ni^{2+}$ (~3 pm difference), allowing them to form an ideal MgO-NiO solid solution.[19-20] Upon reduction, the strong interaction between the Ni atoms and MgO support favors the formation of small, highly dispersed Ni particles, enhancing the catalytic activity.[21]

The most common techniques for the synthesis of DRM catalysts include co-precipitation,[22] and incipient wetness-impregnation methods.[23] Although these methods are very well established due to their simplicity and use of low-cost precursors, they are limited in their ability to controllably produce highly dispersed supported Ni-based catalysts that are coke-resistant.[24] In addition, they require several time-consuming steps including mixing and/or aging, drying, and calcining. Thus, novel synthesis methods have been developed for more rapid and efficient synthesis of coke-resistant, nano-sized catalysts. Methods include modified wet impregnation with non-thermal plasma treatment,[25] atomic layer deposition (ALD),[26] ultrasonic-assisted impregnation,[27] and flame spray pyrolysis.[28] Flame-based aerosol processes are widely used to manufacture nanomaterials such as fumed silica and titania at large scale. In addition, many types of supported noble-metal catalysts have been prepared by these methods.[29-30] Recently, supported non-noble metal catalysts have been synthesized using this technique for the DRM process. Lovell *et al.* prepared mixed silica-ceria-zirconia supports using flame spray pyrolysis and then impregnated Ni onto them.[28] Double flame spray pyrolysis was used to synthesize Ni and Co-based catalysts.[31-32] In all of these prior studies, either the

precursors were relatively expensive organometallic compounds or the metal was decorated onto the support in a separate impregnation process.

Here, we introduce a new flame-based process for one-step, continuous synthesis of supported non-noble metal nanocatalysts from inexpensive aqueous metal salt precursor solutions. We demonstrate the synthesis of Ni-doped MgO (NiMgO-F) nanopowder using a flame-driven high temperature reducing jet (HTRJ) reactor. NiMgO-F particles were formed via a gas-to-particle pathway that generates primary particles below 20 nm in diameter. We employed multiple characterization techniques to study morphology, crystal structure, and catalytic properties of the resulting materials. The NiMgO-F was tested in the DRM process at high space velocities and varying temperatures (from 500°C to 800°C for 4 h each). The catalytic performance was compared with MgO-Ni catalysts prepared by other conventional methods (wet-impregnation and co-precipitation). The stability of the MgO-supported Ni catalyst was tested for 50 h at 700°C, showing minimal deactivation. We also have tested the addition of various possible co-catalysts and promoters, but have found that none improved performance relative to that of the simple MgO-supported Ni catalyst. Overall, this study not only demonstrates a very promising new DRM catalyst, but more broadly demonstrates the potential of this one-step continuous flame-based synthesis approach to produce a wide range of unique multi-component supported non-noble metal catalysts.

## RESULTS AND DISCUSSIONS

### Synthesis, catalytic activity, and characterization of NiMgO-F

**Figure 1** shows a schematic of catalyst production *via* the HTRJ process. Liquid-fed aerosol production processes can produce solid particles by both gas-to-particle and droplet-to-particle conversion mechanisms, depending on the process parameters.[29] In a gas-to-particle conversion process, droplets containing both the support and metal precursors evaporate quickly upon mixing with the hot combustion gases to generate a precursor vapor. Particles then nucleate and grow from gas-phase precursors, which may be converted to the product composition in the gas phase, or after particle nucleation and growth. In droplet-to-particle conversion, reaction primarily takes place in the liquid droplet phase, and each droplet is converted to a single solid particle. Whether gas-to-particle, droplet-to-particle, or a combination of the two occurs depends upon the relative rates of reaction and evaporation. We have previously reported the synthesis of unsupported Ni nanoparticles using this process, and shown that it proceeds by a gas-to-particle conversion process.[33] MgO is not reducible by $H_2$ in the presence of water but some degree of reduction for Ni is likely based on our previous observations. Moreover, the same thermal nozzle technology used in this process is employed by Praxair (now Linde), with more than 2000 times larger gas flow rates, suggesting the scalability of this production technique.[34-36]

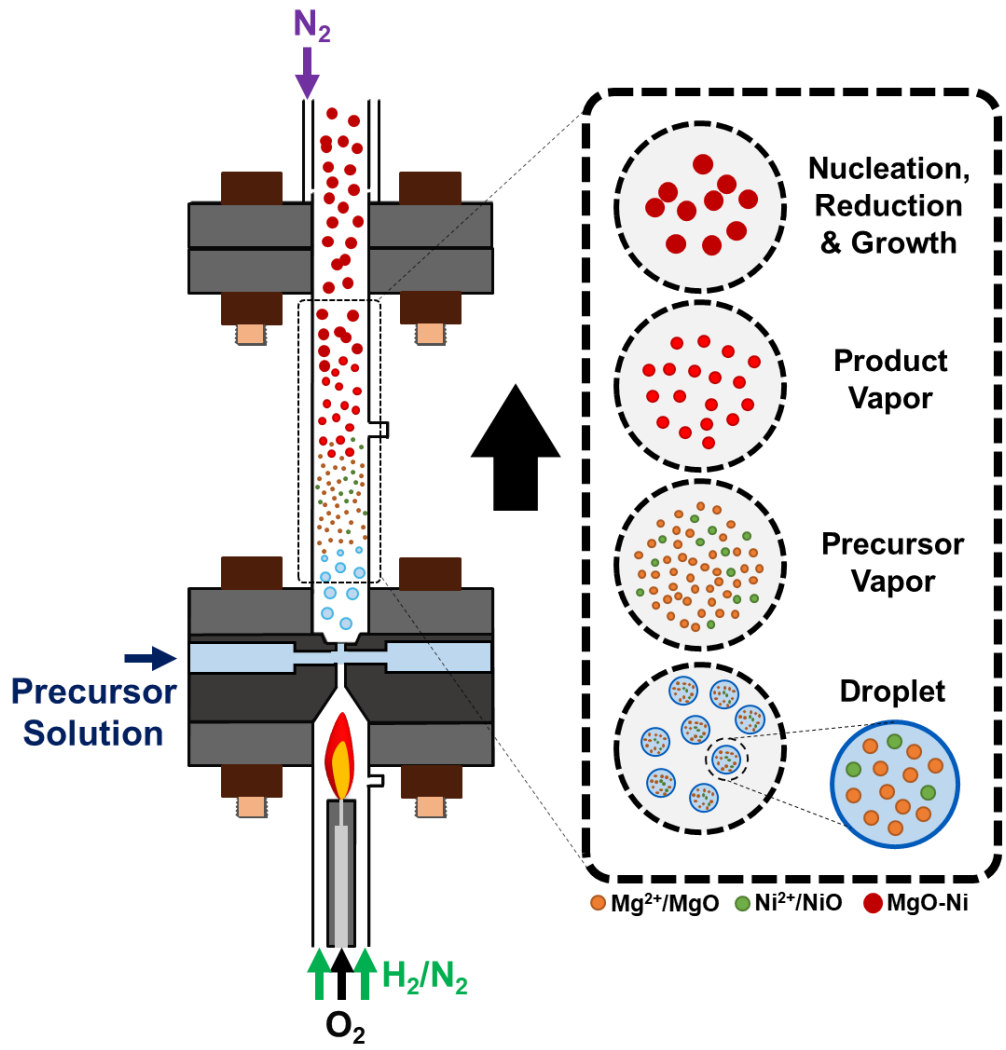


**Figure 1.** Schematic of the HTRJ process: oxygen as oxidant (center), hydrogen as fuel, and nitrogen as inert diluent enter the combustion zone, where they form an inverted diffusion flame above the oxygen inlet orifice; aqueous precursor is injected at the throat section of the converging-diverging nozzle. It is atomized, evaporated, and decomposed upon rapid mixing with the high velocity combustion products. Particles nucleate and grow in the reaction chamber, and catalysts are formed in a reducing environment; synthesized nanoparticles exit the quench zone for downstream collection by filtration or inline sampling for TEM imaging.

Various Ni-based catalysts were synthesized by the HTRJ process and screened for apparent performance in the DRM process (**Figure S1, S2**). Based on the results of this prescreening of possible supports, MgO-supported Ni was selected as the prototypical catalyst for further evaluation here, though other combinations also merit further consideration. Transmission electron microscopy (TEM) images of the as-prepared NiMgO-F nanopowders, sampled directly from the reactor outlet stream, are shown in **Figure 2a,b**. Nanocatalysts with uniform particle sizes are formed by the HTRJ process. The observed modest degree of agglomeration is due to the nature of flame-based methods and the residence time required for catalysts to reach the electrostatic precipitator for TEM sampling. **Figure 2c-e** display a scanning electron microscopy (SEM) image and the corresponding elemental maps for Mg and Ni, respectively. Ni atoms are uniformly dispersed throughout the sample at the resolution of these measurements. The uniform distribution of the active metal at this scale is retained even after heat treatment and reduction (**Figure S3**), suggesting a strong interaction between Ni and the support. X-ray diffraction (XRD) patterns for the support as well as the as-prepared, reduced, and spent catalyst are presented in **Figure 2f**. For the support, all of the peaks can be attributed to cubic periclase MgO (PDF card No. 01-071-1176). As mentioned above, NiO and MgO form an ideal solid solution. Thus, the XRD pattern of NiO (PDF card No. 00-004-0835) is nearly identical to that of MgO, and they cannot readily be distinguished by XRD. However, the higher peak intensities for the Ni-containing catalyst compared with those of the support are consistent with the incorporation of Ni into the MgO, because Ni is expected to scatter x-rays more strongly than Mg. The absence of peaks assignable to metallic Ni, under conditions where NiO would be reduced to Ni, further suggests the

formation of a solid solution.[37-38] For each catalytic experiment, the as-prepared nanocatalyst in the packed bed reactor was first reduced with $H_2$ followed by purging by an inert gas before introducing reactant gases. To observe the differences between the as-prepared nanopowder and the one used in the reaction, the reduced nanocatalyst was also characterized. After reduction, the peaks became sharper than those of the as-prepared catalyst, reflecting some growth of crystallites during heat treatment of the catalyst. The increase in particle size is also evident in TEM images (**Figure S4**). Unlike catalysts prepared by conventional methods, nanoparticles formed in flame-based processes do not undergo long calcination processes. In the HTRJ process, they are only exposed to the high-temperature environment for tens to hundreds of milliseconds. After reduction, the MgO (200) peak was slightly shifted to a lower $2\theta$ position than that of the as-prepared catalyst (42.8° vs. 42.9°). This is consistent with the removal of some Ni atoms from the solid solution.[39] However, no clear diffraction peaks of metallic Ni are visible after the reduction treatment, indicating the high dispersion of Ni nanoparticles in the reduced catalyst.[40] The crystalline size of the spent catalyst after the DRM reaction at four temperatures, is slightly higher than that of the reduced catalyst (~5%), reflecting a small amount of additional sintering during reaction.[41] The Ni peak at around 44° has also become sharper, suggesting additional removal of Ni from the MgO lattice during reaction. Moreover, we observe a broad peak around 25° that was previously absent and that can be attributed to carbon deposited during the DRM reaction. To evaluate the material basicity, $CO_2$-temperature programmed desorption ($CO_2$-TPD) analysis was conducted (**Figure S5**). Both the MgO support and NiMgO-F catalyst have distinct primary peaks attributed to different types of basic sites within the samples. Generally, higher $CO_2$

desorption temperature reflects stronger surface basicity, and therefore stronger ability to adsorb acidic $CO_2$.[42] Here, the peaks below 100°C are related to weak adsorption and the peaks near or above 200°C are attributed to strong adsorption.[43] The BET surface area of the catalyst is 60 $m^2$ $g^{-1}$ (**Figure S6**).

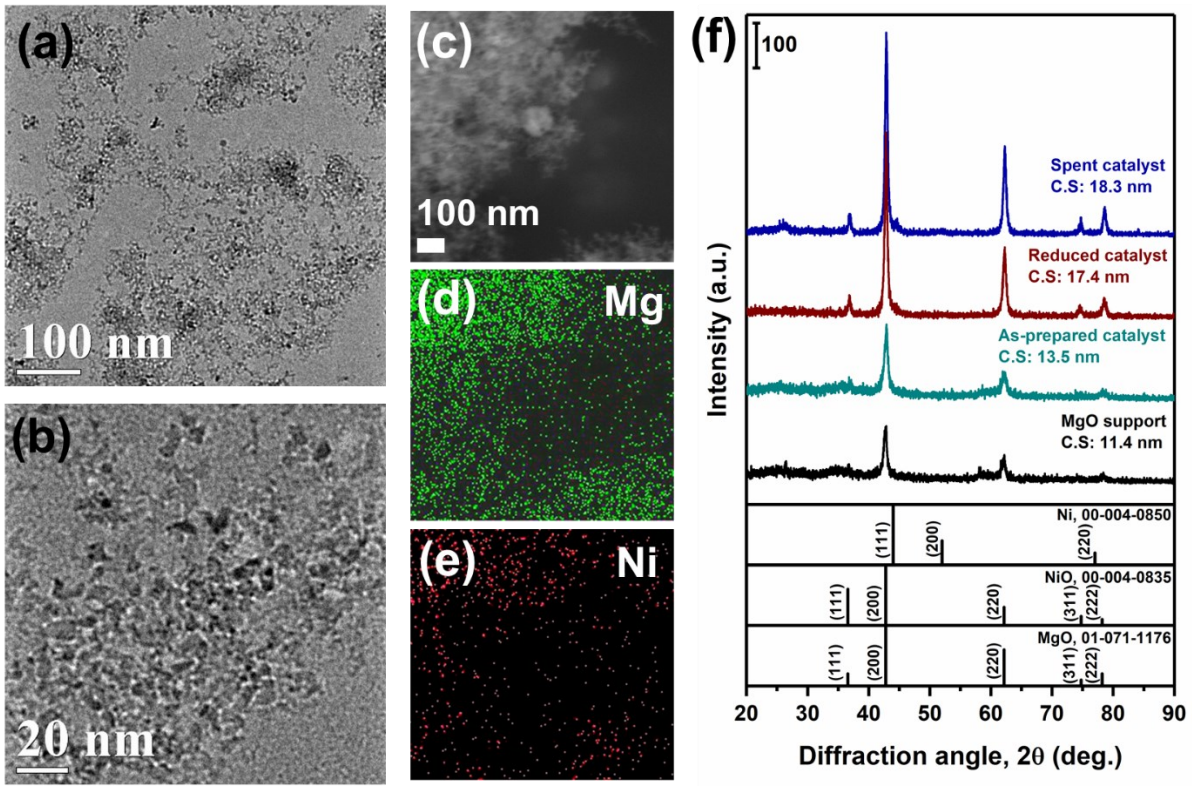


**Figure 2. a,b)** TEM images, and **c)** SEM image of the as-prepared NiMgO-F nanopowders; **d,e)** elemental maps for Mg and Ni, respectively; **f)** XRD patterns of the as-prepared MgO and as prepared, reduced, and spent NiMgO-F nanocatalyst. (C.S: calculated crystalline size).

The activity of NiMgO-F nanocatalyst was evaluated at four different temperatures for 4 h each, as shown in **Figure 3a**. Based on preliminary experiments, Mg:Ni 90:10 wt% was chosen as the optimized composition for the catalyst based on higher overall activity and stability compared with Mg:Ni ratios of 85:15 and 95:5 wt%. For all the temperatures studied, $CO_2$ conversion was higher than $CH_4$ conversion, suggesting the occurrence of reverse water gas shift (RWGS) reaction.[44] At lower temperatures, the conversions are much lower than the equilibrium conversions, consistent with most prior reports for the DRM reaction. However, the numbers are comparable to the $CH_4$ and $CO_2$ conversions reported at low temperatures in other studies.[45] For all temperatures, the $H_2$/CO ratio is less than 1, presumably due to the occurrence of RWGS which consumes $H_2$ while producing CO. The $H_2$/CO ratio varies initially, then becomes stable after about 1 h (**Figure S7**). We note that for all of the temperatures, the catalyst is tested under demanding conditions (flow rate per catalyst mass of 60000 mL $g_{cat}^{-1}$ $h^{-1}$) using a stoichiometric feed without any diluent gases. Results of a recovery test of the catalyst, in which it was cooled back to 500°C while maintaining reactant flows, are shown in **Figure S8**. The low temperature activity recovered to approximately its initial value over a period of about 1 h. In initial screening experiments, the addition of other elements as promoters or co-catalysts did not improve the catalytic activity of the NiMgO-F (**Figure S9, 10**). However, the primary goal of those screening experiments was to demonstrate the flexibility of this single-step process to produce catalysts of diverse compositions, and further study might lead to identification of effective promoters. An apparent activation energy (Ea) for conversion or production of each gas was calculated based on kinetic measurements, as shown in **Figure 3b.** The apparent activation energy for $CO_2$

consumption (21.9 kJ $mol^{-1}$) was lower than that of $CH_4$ consumption (24.9 kJ $mol^{-1}$)). This is consistent with other reports of methane activation being the rate-determining step in the dry reforming of methane, under conditions where RWGS is minimized.[46-48] Moreover, $H_2$ production had the largest apparent activation energy (33.0 kJ $mol^{-1}$). Recently, the apparent activation energies of nickel-based catalysts reported in the literature have been compared.[49] In all cases, the apparent activation energy for $H_2$ production was the largest. In addition, the numbers were in the range of ~20-150 kJ $mol^{-1}$. Although each catalyst, with a different support, was tested for specific conditions, which limits the ability to draw conclusions from direct comparisons, NiMgO-F falls among the lower values of apparent activation energy, consistent with its high activity for the DRM reaction. The experiments were replicated at other gas flowrate to catalyst mass ratios (**Figure S11**), and the calculated numbers were within ±10% of the apparent activation energies presented here.

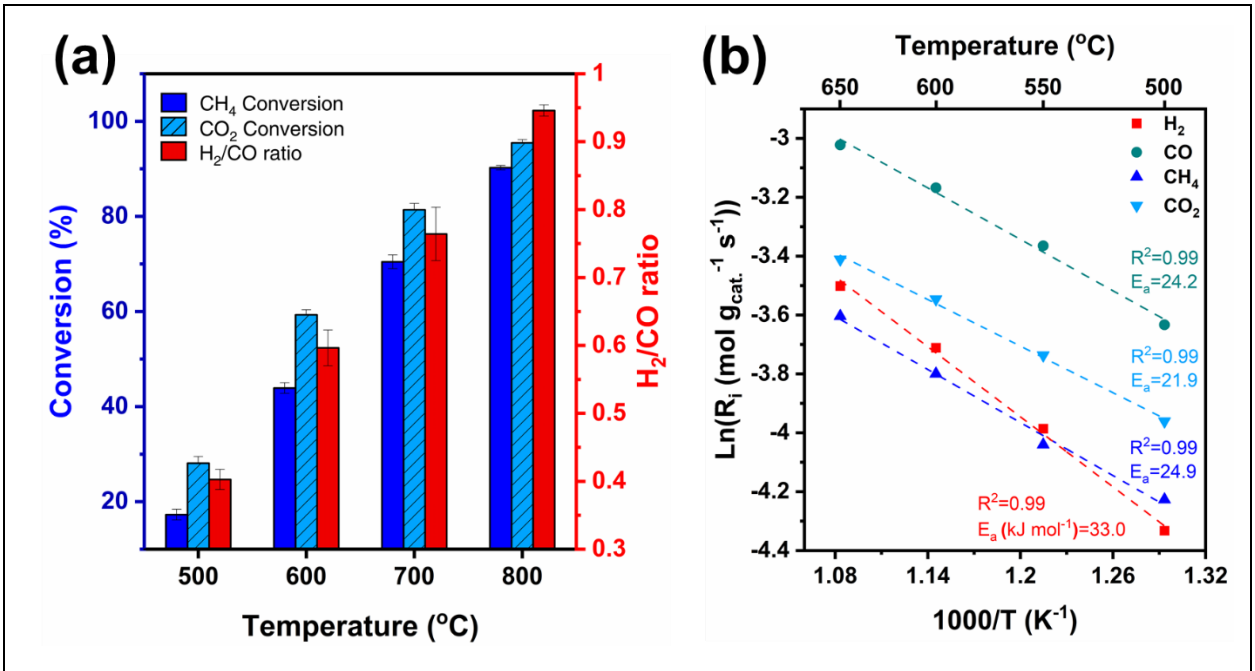


**Figure 3. a)** The activity of NiMgO-F catalyst at 4 temperatures. (gas flow to catalyst mass ratio: 60000 mL $g_{cat}^{-1}$ $h^{-1}$, no diluent gas). Methane equilibrium conversions

considering C deposition, ethane and ethylene formation (negligible, but included for completeness), and RWGS: 500°C: 70.9%, 600°C: 82.3%, 700°C: 91.5%, 800°C: 96.3%.[50] All values are mean ± standard deviation; **b)** Arrhenius plot for extracting apparent activation energy for each gas by calculating the reaction rates at each temperature (500, 550, 600, 650°C). (gas flow to catalyst mass ratio: 240,000 mL $g_{cat}^{-1}$ $h^{-1}$, 1:1:2 $CH_4$, $CO_2$, Ar).

**Comparison of catalytic activity of NiMgO catalysts prepared by different methods**

The catalytic activities of four NiMgO catalysts are compared: NiMgO-F, NiMgO-FI, NiMgO-CI, and NiMgO-CP (**Figure S12-14**). **Figure 4a,b** shows $CH_4$ conversion and $H_2$/CO ratio produced using the four catalysts at different temperatures. Prior studies have shown that catalysts prepared by different techniques exhibit different activities as observed here.[16] Among all the catalysts, NiMgO-CI was the least active material on a catalyst mass basis. Comparing the activity of NiMgO-FI and NiMgO-CI suggests that the size and morphology of the support are essential, as well as the means of depositing the active metal. The low activity of NiMgO-CI can be due to the larger particle size of the commercial MgO compared to the MgO produced by the HTRJ process (**Figure S15**) and the relatively low dispersion of Ni on the NiMgO-CI compared to the NiMgO-FI (**Table 1)**. Thus, both the support surface area and Ni surface area are relatively low for NiMgO-CI. NiMgO-F and NiMgO-FI catalysts show comparable performance, with higher activity of NiMgO-F at low temperatures and slightly higher activity of NiMgO-FI at high temperatures, but these differences are small. Moreover, the NiMgO-FI produces higher $H_2$/CO ratio at high temperatures. On the other hand, TGA results show the highest weight

loss for NiMgO-FI spent catalyst, which mainly originates from carbon deposition due to $CH_4$ decomposition and CO disproportionation (**Figure 4c**).[41] Although NiMgO-F has the second most weight loss, more of this weight loss occurs at lower temperature (compared with the sharp weight loss of NiMgO-FI at high temperature). This suggests that much of the deposited carbon is relatively reactive amorphous and whisker rather than more graphitic, unreactive carbons that are responsible for deactivation. The lower weight loss of spent NiMgO-CI and NiMgO-CP may simply reflect their lower activity than the other two samples. That is, they are less active for carbon deposition, but also less active for the desired reaction, and these activities are correlated, particularly given that activity measured in terms of $CH_4$ conversion includes a contribution from carbon deposition. As mentioned earlier, the reaction occurs at a relatively high space velocity, and the residence time is insufficient for gasification of all carbon deposits.[44] For each of the spent catalysts, except for NiMgO-F, the formation of carbon nanotubes or fibers was observed in TEM imaging (**Figure 4d-g**). Such one-dimensional carbon deposits were not found in the spent NiMgO-F catalyst. The Ni in NiMgO-F may be more deeply embedded in the MgO structure than in the other samples, preventing the formation of tubes and fibers that grow from discrete nickel nanoparticles on the support surface.

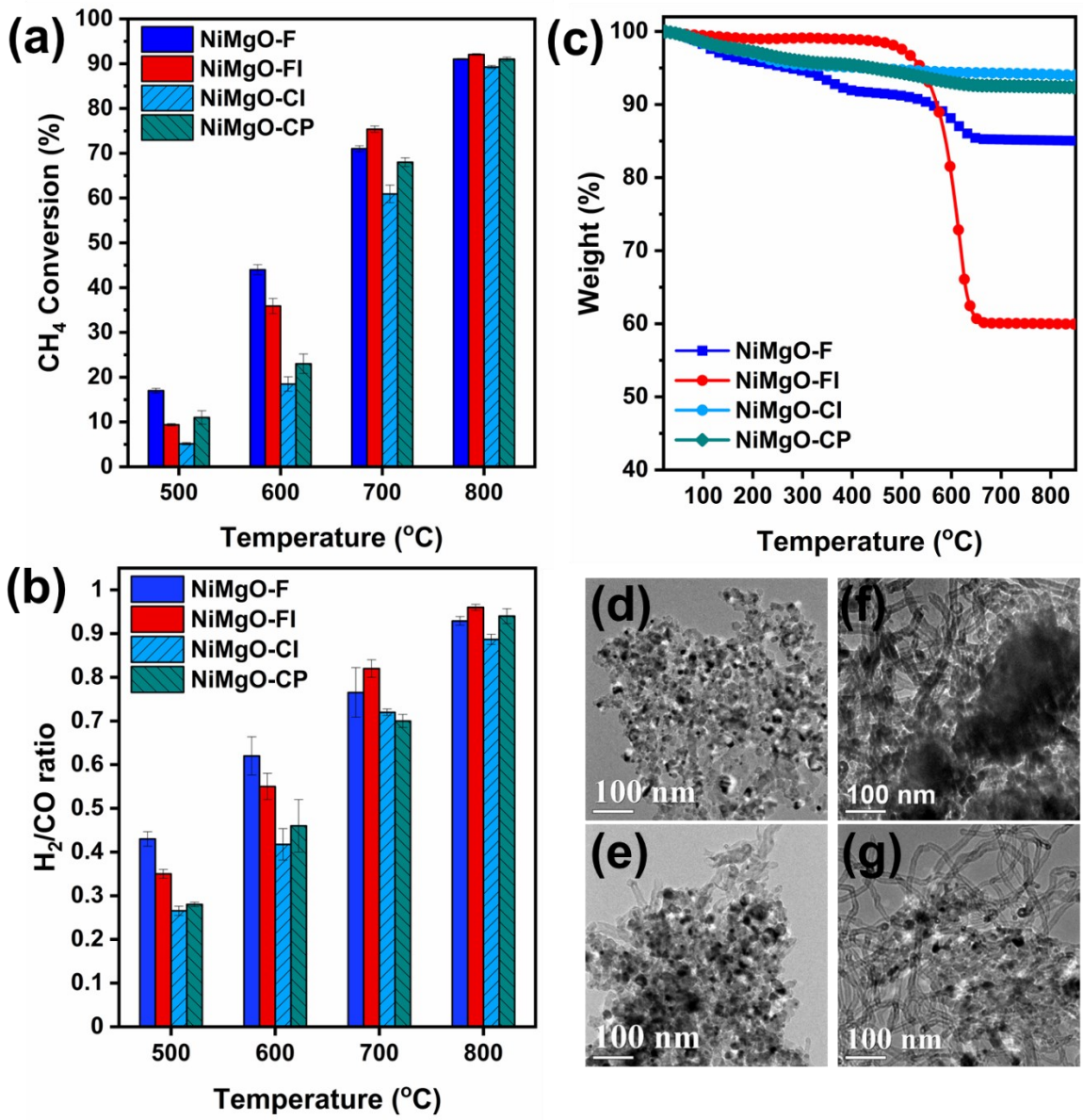


**Figure 4. a)** $CH_4$ conversion; and **b)** $H_2/CO$ ratio for the four catalysts at four temperatures (feed flow to catalyst mass ratio: 60000 mL $g_{cat}^{-1}$ $h^{-1}$, no diluent gas); **c)** weight losses, and **d-g)** TEM images of the spent catalysts (d: NiMgO-F, e: NiMgO-FI, f: NiMgO-CI, g: NiMgO-CP). All values are mean ± standard deviation.

**Table 1** presents results of detailed characterization of NiMgO catalysts prepared by different methods. Mg/Ni wt. ratios for all the samples are within the expected ranges.

The Mg/Ni wt. ratio for NiMgO-FI is slightly lower than expected, which may simply be due to instrument error and/or the specific locations taken for the analysis. The HTRJ process is generally capable of producing multicomponent nanomaterials with controlled compositions as reported before.[51] NiMgO-CI has the largest crystallite and calculated particle size, consistent with the larger size of the commercial MgO used for the synthesis, as observed by TEM. $H_2$ consumption and reduction degree are calculated based on the $H_2$-TPR curves presented in **Figure S16**. NiMgO-F consumes the least amount of $H_2$ among all the samples, with no sharp peaks. MgO-supported Ni catalysts are reported to form complete solid solutions at low Ni compositions after calcining at high temperatures.[52] High calcination temperature has a strong influence on the diffusion of NiO into the NiO−MgO solid solution.[41] In addition, as mentioned earlier, some degree of reduction takes place in the reaction chamber due to the presence of excess $H_2$ and therefore, pre-reduced catalysts are formed. In all the other samples, the $H_2$ consumption at lower temperature (peaks or shoulders) is due to the reduction of $Ni^{2+}$ located at the surface of the catalyst and/or to the reduction of NiO uninfluenced by the MgO support; at higher temperatures, NiO species with strong interactions with MgO are reduced.[41, 44] Upon formation of NiO-MgO solid solution, the peak corresponding to bulk NiO usually shifts to higher temperature, and the reduction of $Ni^{2+}$ becomes more difficult. Thus, the broad consumption of hydrogen at ~800°C for NiMgO-FI and NiMgO-CI might be attributed to the reduction of $Ni^{2+}$ cations inserted into the lattice of MgO.[39] For NiMgO-FI, the reduction degree is more than 100%, suggesting that either the actual Ni content used in the catalyst was more than the theoretical value (6.3 wt%) or there was a reducible impurity in the sample for $H_2$-TPR analysis. The high turnover frequency and low Ni

apparent dispersion of the NiMgO-F catalyst can also be caused by the formation of NiO-MgO solid solution and resulting inaccessible Ni atoms within the bulk of the MgO. That is, here we are using the term dispersion in the way it is usually applied in heterogeneous catalysis, as the fraction of the active metal that is available for reaction. However, in the usual case, this is simply related to the specific surface area of the metal deposited on the support. Here, because an unknown amount of nickel may remain incorporate within the MgO phase, the dispersion is not simply dependent upon the size of nickel clusters or particles on the surface. The turnover frequencies computed based upon the nickel surface area measured by CO chemisorption are given in **Table 1**. The high activity, per catalyst mass, of NiMgO-F combined with low Ni surface area leads to a computed turnover frequency that is much higher than for the other catalysts. This may imply that the active sites on NiMgO-F, though fewer in number, are much more active than those of the other catalysts. However, we cannot rule out the possibility that additional active sites are generated under reaction conditions that are not observed by CO uptake at 35°C.

**Table 1.** Detailed characterization of NiMgO catalysts prepared by different methods

| | NiMgO-F | NiMgO-FI | NiMgO-CI | NiMgO-CP |
|---|---|---|---|---|
| Elemental composition[1] (Mg/Ni wt. ratio) | 9.2±0.5 | 7.2±0.7 | 8.8±1.6 | 8.8±0.5 |
| Crystalline size[2] (nm) | 13 | 11 | 17 | 8 |
| Calculated particle size[3] (nm) | 3.7 | 8.6 | 17.5 | 5.7 |
| $H_2$ consumption[4] (cc $g^{-1}$) | 2.56 | 30.14 | 20.07 | 15.5 |
| Reduction degree[5] (%) | 10.7 | 125.6 | 83.6 | 64.6 |
| Turnover frequency at 500°C[6] ($s^{-1}$) | 25.9 | 1.65 | 4.06 | 3.27 |
| Ni Dispersion[6] (%) | 0.23 | 1.97 | 0.44 | 1.17 |

| | | | | |
|---|---|---|---|---|
| Ni surface area[6] ($m^2$ $g^{-1}$) | 0.095 | 0.83 | 0.19 | 0.49 |

[1] Elemental composition is determined based on EDS analysis. All values are mean ± standard deviation.
[2] Crystallite size is calculated based on broadening of the MgO (200) peak in the XRD patterns.
[3] Particle size (geometric mean diameter) is calculated based on the processing of TEM images provided in **Figure S17**.
[4] $H_2$ consumption and reduction percentage are calculated based on the $H_2$-TPR analysis.
[5] Reduction degree is calculated based on the 6.3 wt% theoretical Ni content of the catalyst.
[6] Turnover frequency, Ni dispersion, and Ni surface area are calculated based on the results of CO chemisorption analysis.

**Stability study of NiMgO-F nanocatalyst**

In this section, the NiMgO-F catalyst was selected for further study. The stability of the catalyst was tested at 700°C for 50 h. **Figure 5** displays the $CH_4$ and $CO_2$ conversion, $H_2$/CO ratio, and $H_2$ yield of the catalyst over time in the DRM reaction. Initially, the $H_2$/CO ratio and $H_2$ yield for the NiMgO-F catalyst dropped, while the $CH_4$ and $CO_2$ conversions remained relatively stable. Decreased $H_2$ yield at fixed $CH_4$ and $CO_2$ conversions should be accompanied by increased C deposition by a combination of RWGS and the Bouduard reaction, which together convert CO and $H_2$ to C and $H_2O$. Eventually, carbon deposition may deactivate sites that are active for RWGS, and the $H_2$ yield recovers. NiMgO-F shows quite stable activity over time with a $H_2$ yield close to 70% (equilibrium $H_2$ yield: 75.9%) throughout.

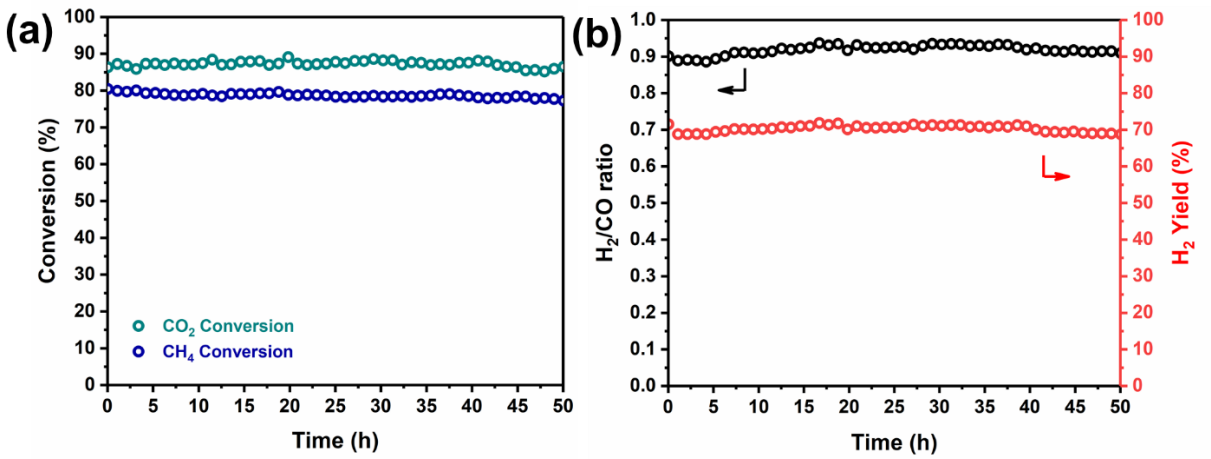


**Figure 5.** The stability of NiMgO-F catalyst for 50 h: **a)** $CH_4$ and $CO_2$ conversions; **b)** $H_2$/CO ratio and $H_2$ yield. (feed flow to catalyst mass ratio: 18000 mL $g_{cat}^{-1}$ $h^{-1}$, no diluent gas). Equilibrium $H_2$ yield is 75.9%.[50]

Spent NiMgO-F catalyst was further characterized after the 50 h stability test. **Figure 6a,b** display TEM images of the spent catalyst. As mentioned earlier, no carbon nanotubes or nanofibers are observed for the NiMgO-F spent samples, even after 50 h on stream. We attribute this resistance to carbon filament growth to the formation of NiO-MgO solid solution and strong interaction between the active metal and support. To investigate the type of carbon formed during the DRM reaction, $O_2$-TPO analysis was conducted (**Figure 6c**). In addition to $CO_2$ formation, CO formation was recorded as a function of temperature (**Figure S18**). Peaks at low temperatures in both $CO_2$ and CO formation graphs are attributed to the oxidation of active carbon species, which is mainly attributed to the presence of amorphous carbon. However, the peak at 629°C corresponds to the oxidation of less active (graphitic) carbon species, which are generally associated with deactivation of the catalyst.[53] The weight loss of the spent catalyst after heating to 900°C was ~20% according to the TGA analysis (**Figure S19**). The Raman spectrum of the sample shown

in **Figure 6d** displays three distinct peaks corresponding to D, G, and 2D bands. The G-band is attributed to $sp^2$-hybridized C atoms, and the D-band is assigned to defects in carbon materials.[54] The band intensity ratio of G and D bands, $I_G/I_D$, which reflects the graphitic degree of carbon on the catalyst surface, is below 1, indicating the presence of both amorphous and graphitized carbons. Moreover, the presence of a sharp 2D peak indicates that the carbon layer is quite thin.

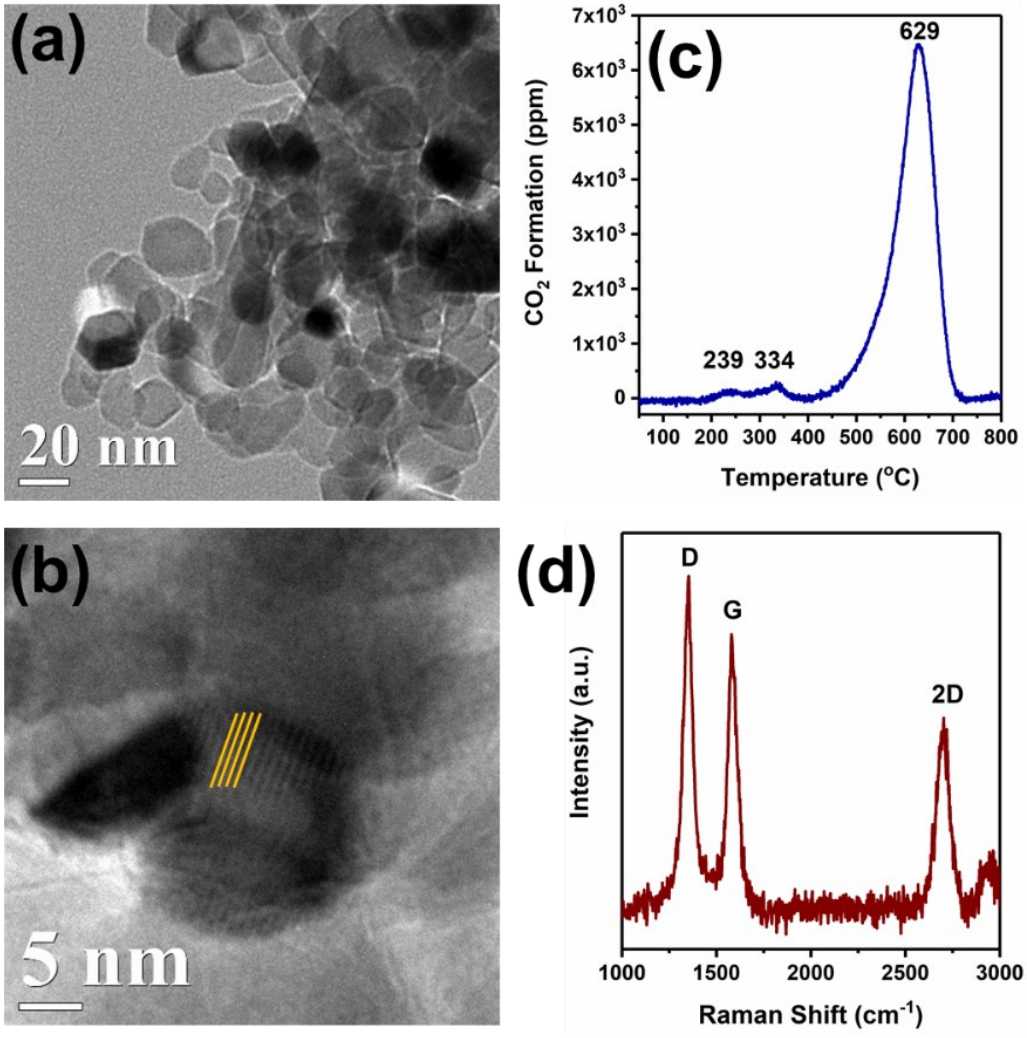


**Figure 6.a,b)** TEM images; **c)** $CO_2$ formation during $O_2$-TPO; and **d)** Raman spectrum of the spent NiMgO-F after 50 h stability test.

## CONCLUSION

We presented the production of MgO-supported Ni-based catalysts using the flame-based HTRJ aerosol reactor. The NiMgO-F nanocatalyst was synthesized using a one-step, continuous process from an aqueous solution of inexpensive aqueous metal nitrate precursors. According to TEM images, nanopowders were <20 nm in average size. Elemental maps showed the uniform distribution of active metal in the support. XRD patterns confirmed the formation of MgO-NiO solid solutions with sharper peaks for the catalyst compared to the peaks of the support material alone. The NiMgO-F nanocatalyst showed high activity and stable performance in the DRM reaction from 500 to 800°C. The calculated apparent activation energies for reactants and products were in the range of ~20-40 kJ $mol^{-1}$ with a smaller value for $CO_2$ consumption compared with $CH_4$ consumption, indicating a higher barrier to $CH_4$ activation than $CO_2$ activation. Compared with catalysts prepared by other methods (NiMgO-FI, NiMgO-CI, NiMgO-CP), the NiMgO-F catalyst showed particularly high activity at temperatures below 700°C. Comparing the two catalysts prepared with the same recipe but using different support sources (MgO from HTRJ and commercial MgO nanopowder) revealed that the size and morphology of the support play an important role in the catalytic activity, and that the HTRJ process can produce unique and advantageous support morphologies. NiMgO-FI performed better than the NiMgO-CI probably due to the smaller particle size of MgO produced by the HTRJ process. The NiMgO-F was tested in a stability test. The nanocatalyst was stable with almost constant $H_2$ production over time. The detailed characterization of NiMgO-F spent catalyst after the stability test confirmed the presence of both amorphous and

graphitic carbon without the formation of carbon nanotubes or nanofibers. This study demonstrated the potential of a one-step continuous flame-based aerosol synthesis approach to produce a wide range of unique supported non-noble metal nanocatalysts, including a particular example with competitive performance in the DRM reaction.

# EXPERIMENTAL SECTION

## Materials

Nickel nitrate hexahydrate (ACROS Organics, 99%) and magnesium nitrate (Sigma Aldrich, 99%) were used as catalyst precursors. For the synthesis, hydrogen (Industrial grade), oxygen (Industrial grade), and liquid nitrogen were obtained from Airgas, an Air Liquide company. For the catalyst activity tests, argon (ultra-high purity grade, 99.999%), hydrogen (industrial grade), methane (chemically pure grade, 99.5%), and carbon dioxide (bone dry grade, 99.9%) from Airgas were used. A 293 mm polyvinylidene fluoride (PVDF) filter membrane of 220 nm nominal pore size (Millipore-Sigma) was used for nanocatalyst collection.

## Synthesis of NiMgO-F nanocatalyst

MgO-supported Ni nanopowders (NiMgO-F) were synthesized at a production rate of ~250 mg $h^{-1}$ using the HTRJ process, as described in detail previously [55-56]. A schematic of the process is shown in **Figure S20**. In this continuous process, combustion products of a hydrogen-rich flame ($H_2$: 17 Standard Liters per Minute-SLM, $O_2$: 4 SLM, $N_2$: 8 SLM) passed through a converging-diverging nozzle. An aqueous solution (25 mM) of precursors containing Ni and Mg nitrates was injected (250 mL $h^{-1}$) by a peristaltic pump (Tris, ISCO) at the throat section of the nozzle. The mass ratio of Mg to Ni in the precursor was fixed at 9. The precursor solution was atomized by the hot high-velocity gas stream and the resulting droplets evaporated in the reducing environment of the reaction chamber containing excess $H_2$ at high temperature (≈600°C to 650°C). Downstream from the reaction zone, the products were cooled immediately by a nitrogen quench flow (100

SLM) and collected on a filter membrane. The synthesis of MgO-supported Ni catalysts prepared by other methods is described in the supporting information.

**Materials characterizations**

The size and morphology of MgO-supported Ni nanopowders were characterized using a JEOL JEM 2010 Transmission Electron Microscope (TEM) at 200 kV working voltage. 200-mesh copper TEM grids with a carbon support film (Ted Pella) were used for the analysis. To observe the morphology of the as-prepared NiMgO-F nanoparticles, a custom-built electrostatic sampler connected to the HTRJ process was used to collect samples directly from the aerosol product stream onto TEM grids for offline analysis. For the rest of the nanopowders, including the reduced NiMgO-F, spent NiMgO-F, and catalysts prepared by other methods, dry samples were taken by sliding the carbon-coated TEM grid on the dry powder. ImageJ software was used to estimate the particle size distribution of nanoparticles. The morphology and elemental composition of catalysts were characterized using a Cross-Beam® Focused Ion Beam-Scanning Electron Microscopy (FIB-SEM) Workstation (Carl Zeiss AURIGA) with an Energy Dispersive X-ray Spectroscopy (EDS) detector (Oxford Instruments, X-Max® 20 $mm^2$). The crystal structure of samples was determined by X-ray Diffraction (XRD) analysis (Rigaku Ultima IV with Cu Kα X-ray source). The crystalline size of the samples was estimated by the Debye−Scherrer equation based on the Mg (200) peak of the XRD patterns. Raman spectroscopy, using a Renishaw system with 514 nm excitation laser focused through a 20× microscope objective, was employed at room temperature to determine the graphitization degree of carbon present in the spent catalysts. To determine the carbon amount in the spent catalysts, thermogravimetric analysis (TA instruments DSC SDT

Q600) was conducted in air from room temperature to 900°C at a heating rate of 10°C $min^{-1}$. The Brunauer-Emmett-Teller (BET) surface area of NiMgO-F nanocatalyst was measured by $N_2$ adsorption-desorption at 77 K (Micromeritics Tri-Star II). Before the test, the sample was degassed at 150°C under vacuum for 3 h. $H_2$ temperature-programmed reduction ($H_2$-TPR) and CO pulse chemisorption were conducted on a Micromeritics AutoChem II 2920 instrument.[57] In each of these tests, each catalyst (~50 mg) was loaded in a U-shaped quartz tube reactor. For $H_2$-TPR, the catalyst was first pretreated in 50 sccm Ar (Airgas, ultra-high purity grade) for 1 h at 500°C. The catalyst was then cooled to room temperature before introducing 50 sccm of 10% $H_2$/Ar (Airgas, ultra-high purity grade). Afterward, the catalyst temperature was increased from room temperature to 1000°C at a heating rate of 10°C $min^{-1}$. For CO pulse chemisorption, each catalyst was first reduced under 10% $H_2$/Ar (50 sccm) at 700°C for 1h, followed by cooling to 35°C under Ar (50 sccm). Finally, several pulses of 10% CO/He (Airgas, ultra-high purity grade) were injected into the sample until no further CO uptake was observed. The amount of available surface Ni sites was calculated based on the cumulative CO uptake assuming a 1:1 stoichiometric ratio of CO:Ni surface sites. $CO_2$ TPD was conducted in a custom-built microreactor to determine the basicity of NiMgO-F. 50 mg of catalyst was first reduced by 10% $H_2$/Ar (50 sccm) at 700°C for 1 h, followed by cooling to room temperature under pure Ar (50 sccm). Then the catalyst surface was saturated with 100% $CO_2$ (50 sccm) for 1 h. After that, 50 sccm Ar was introduced to remove physisorbed $CO_2$. Finally, the catalyst was heated from room temperature to 1000°C at a heating rate of 10°C $min^{-1}$ under Ar (50 sccm). The $CO_2$ (m/z = 44) desorption profile was recorded with a mass spectrometer (Pfeiffer Omnistar GSD 320). Oxygen temperature-programmed

oxidation ($O_2$-TPO) was performed in a custom-built microreactor equipped with an MKS FTIR gas analyzer (Multigas 2030), as reported previously.[58] 25 mg of spent catalyst was first pretreated under pure Ar (100 sccm) at 150°C for 30 min and then the catalyst was cooled to room temperature. Next, the catalyst was heated to 800°C at a ramping rate of 10°C $min^{-1}$ under 20% $O_2$/Ar (100 sccm). CO and $CO_2$ formation during the TPO process was recorded by the MKS FTIR gas analyzer with appropriate measurement ranges for CO (0-500 ppm) and $CO_2$ (0-20%).

**Catalytic activity tests**

The catalytic activity of the catalysts was evaluated at atmospheric pressure using a continuous fixed-bed flow reactor (inner diameter of 4 mm) (**Figure S21**). For all the experiments except the stability test, the catalyst (50 mg) was loaded in the quartz tube between plugs of quartz wool. $CH_4$ and $CO_2$ at an equal molar ratio (25 cc per minute (ccm) each, based on nominal ambient conditions of 293 K and 1 bar, corresponding to ~23.3 sccm) and without any dilution were introduced to the reactor. This relatively high feed flow rate per total catalyst mass of 60,000 mL $g_{cat}^{-1}$ $h^{-1}$ was employed to observe differences in catalyst activities even for highly active catalysts. This ensures that, at least for the lower temperatures, the reaction does not closely approach equilibrium, which would obscure differences in performance between catalysts. In all cases, the catalyst was used as a bed of nonporous moderately-aggregated nanopowder, which rules out transport limitations that might be a concern for a pelletized catalyst or larger particles of nanoporous material. The catalyst was reduced in the reactor under a $H_2$:Ar 1:1 50 ccm total flow at 700°C for 1 h prior to testing. The catalytic tests were carried out from 500°C to 800°C in 100°C increments with a ramp rate of 10°C $min^{-1}$. At each step, the system

was held for 0.5 h as 12 samples were taken for GC analysis. For stability tests, the gas flowrate to catalyst mass ratio was reduced to 18000 mL $g_{cat}^{-1}$ $h^{-1}$ by supplying 15 ccm of each reactant and using 100 mg catalyst, and the reactor was held at 700°C for 50 h. For all the experiments, the products and unreacted gases were analyzed on-line by a gas chromatograph (SRI 8610) with a Restek Natural Gas ShinCarbon ST (micropacked) column followed by an oxidizer and a TCD. The oxidizer converts $H_2$ to $H_2O$ and CO to $CO_2$, after they have been separated in the column, allowing quantification of CO from $CO_2$ calibrations. A known flow of $H_2$ was used for calibration, but detection as $H_2O$ provided more sensitive and reliable detection by the TCD. Independent measurements with a second TCD channel showed that methane did not react in the oxidizer. The conversion of reactants, $H_2$/CO ratio, and $H_2$ yield were calculated by the following **Equations 4-7**:

$$X_{CH_4} = \frac{F_{CH_4,\,in} - F_{CH_4,\,out}}{F_{CH_4,\,in}} \times 100 \qquad (4)$$

$$X_{CO_2} = \frac{F_{CO_2,\,in} - F_{CO_2,\,out}}{F_{CO_2,\,in}} \times 100 \qquad (5)$$

$$\frac{H_2}{CO} = \frac{F_{H_2,\,out}}{F_{CO,\,out}} \qquad (6)$$

$$H_2\ yield\ (\%) = \frac{F_{H_2,\,out}}{2F_{CH_4,\,in}} \times 100 \qquad (7)$$

where $X$ is conversion, and $F$ is the flow rate. A mass flow meter at the reactor outlet allows measurement of total gas outflow and thereby conversion of the composition measurement from the GC to total flows of each component, even under conditions where carbon deposition occurs in the reactor.

Kinetic measurements were conducted in the temperature range of 500-650°C (50°C intervals) at reaction conditions far from equilibrium (conversions <15%). The gas flowrate to catalyst mass ratio was increased to 240,000 mL $g_{cat}^{-1}$ $h^{-1}$ by supplying 25 ccm of each reactant, 50 ccm of argon and using 25 mg NiMgO-F catalyst. The catalyst mass-basis reaction rates were calculated by the following **Equations 8,9**:

$$r_{CH_4,CO_2}\ (mol\ g^{-1}s^{-1}) = \frac{F_{i,\ in} \times X_i}{1000 \times 22.4 \times 60 \times W_{cat.}} \times 100 \qquad (8)$$

$$r_{H_2,CO}\ (mol\ g^{-1}s^{-1}) = \frac{F_{i,\ out}}{1000 \times 22.4 \times 60 \times W_{cat.}} \times 100 \qquad (9)$$

Where $F_i$ and $X_i$ are the flow rate and conversion of component *i*, respectively and $W_{cat.}$ is the mass of catalyst (25 mg). The apparent activation energy for each gas was calculated as the slope of an Arrhenius plot of the logarithm of rate vs. inverse temperature times the negative of ideal gas constant (*R*).

## ASSOCIATED CONTENT

### Supporting Information

Supporting information available: Synthesis procedures of NiMgO-FI, NiMgO-CI, NiMgO-CP catalysts, Ni dispersion and surface area equations, flame-made Ni catalyst activity using different supports, co-catalysts and promoters, SEM and TEM images of catalysts, TGA, BET and catalytic characterizations of catalysts, schematics of the HTRJ process and catalyst testing setup.

## ACKNOWLEDGMENT

This work was supported by the National Science Foundation, grant number CBET-1804996.

## References


(1) Pan, F.; Xiang, X.; Du, Z.; Sarnello, E.; Li, T.; Li, Y. Integrating Photocatalysis and Thermocatalysis to Enable Efficient $CO_2$ Reforming of Methane on Pt Supported $CeO_2$ with Zn Doping and Atomic Layer Deposited MgO Overcoating. *Appl. Catal., B* **2020,** 260, 118189.

(2) Li, X.; Li, D.; Tian, H.; Zeng, L.; Zhao, Z.-J.; Gong, J. Dry Reforming of Methane Over Ni/$La_2O_3$ Nanorod Catalysts with Stabilized Ni Nanoparticles. *Appl. Catal., B* **2017,** 202, 683-694.

(3) Abdulrasheed, A.; Jalil, A. A.; Gambo, Y.; Ibrahim, M.; Hambali, H. U.; Shahul Hamid, M. Y. A Review on Catalyst Development for Dry Reforming of Methane to Syngas: Recent Advances. *Renewable Sustainable Energy Rev.* **2019,** 108, 175-193.

(4) Yentekakis, I. V.; Goula, G.; Hatzisymeon, M.; Betsi-Argyropoulou, I.; Botzolaki, G.; Kousi, K.; Kondarides, D. I.; Taylor, M. J.; Parlett, C. M.; Osatiashtiani, A. Effect of Support Oxygen Storage Capacity on the Catalytic Performance of Rh Nanoparticles for $CO_2$ Reforming of Methane. *Appl. Catal., B* **2019,** 243, 490-501.

(5) Zhang, J.-C.; Ge, B.-H.; Liu, T.-F.; Yang, Y.-Z.; Li, B.; Li, W.-Z. Robust Ruthenium-Saving Catalyst for High-Temperature Carbon Dioxide Reforming of Methane. *ACS Catal.* **2020**, 10, 783-791.

(6) Araújo, J. C.; Oton, L. F.; Bessa, B.; Neto, A. B.; Oliveira, A. C.; Lang, R.; Otubo, L.; Bueno, J. M. The Role of Pt Loading on $La_2O_3$-$Al_2O_3$ Support for Methane Conversion Reactions via Partial Oxidation and Steam Reforming. *Fuel* **2019,** 254, 115681.

(7) Paksoy, A. I.; Caglayan, B. S.; Aksoylu, A. E. A Study on Characterization and Methane Dry Reforming Performance of Co–Ce/$ZrO_2$ Catalyst. *Appl. Catal., B* **2015,** 168-169, 164-174.

(8) Sheng, K.; Luan, D.; Jiang, H.; Zeng, F.; Wei, B.; Pang, F.; Ge, J. $Ni_xCo_y$ Nanocatalyst Supported by $ZrO_2$ Hollow Sphere for Dry Reforming of Methane: Synergetic Catalysis by Ni and Co in Alloy. *ACS Appl. Mater. Interface* **2019,** 11 (27), 24078-24087.

(9) Li, M.; van Veen, A. C. Tuning the Catalytic Performance of Ni-catalysed Dry Reforming of Methane and Carbon Deposition via Ni-$CeO_{2-x}$ Interaction. *Appl. Catal., B* **2018,** 237, 641-648.

(10) Theofanidis, S. A.; Galvita, V. V.; Poelman, H.; Marin, G. B. Enhanced Carbon-Resistant Dry Reforming Fe-Ni Catalyst: Role of Fe. *ACS Catal* **2015,** 5 (5), 3028-3039.

(11) Kroll, V. C. H.; Swaan, H. M.; Lacombe, S.; Mirodatos, C. Methane Reforming Reaction with Carbon Dioxide over Ni/$SiO_2$ Catalyst: II. A Mechanistic Study. *J. Catal.* **1996,** 164 (2), 387-398.

(12) Pakhare, D.; Spivey, J. A Review of Dry ($CO_2$) Reforming of Methane Over Noble Metal Catalysts. *Chem. Soc. Rev.* **2014,** 43 (22), 7813-7837.

(13) Ferreira-Aparicio, P.; Rodríguez-Ramos, I.; Anderson, J. A.; Guerrero-Ruiz, A. Mechanistic Aspects of the Dry Reforming of Methane Over Ruthenium Catalysts. *Appl. Catal., A* **2000,** 202 (2), 183-196.

(14) Kawi, S.; Kathiraser, Y.; Ni, J.; Oemar, U.; Li, Z.; Saw, E. T. Progress in Synthesis of Highly Active and Stable Nickel-Based Catalysts for Carbon Dioxide Reforming of Methane. *ChemSusChem* **2015,** 8 (21), 3556-3575.

(15) Han, J. W.; Park, J. S.; Choi, M. S.; Lee, H. Uncoupling the Size and Support Effects of Ni Catalysts for Dry Reforming of Methane. *Appl. Catal., B* **2017,** 203, 625-632.

(16) Hu, Y. H.; Ruckenstein, E. Binary MgO-based Solid Solution Catalysts for Methane Conversion to Syngas. *Catal. Rev.* **2002,** 44 (3), 423-453.

(17) Alipour, Z.; Rezaei, M.; Meshkani, F. Effect of Alkaline Earth Promoters (MgO, CaO, and BaO) on the Activity and Coke Formation of Ni Catalysts Supported on Nanocrystalline $Al_2O_3$ in Dry Reforming of Methane. *J. Ind. Eng. Chem.* **2014,** 20 (5), 2858-2863.

(18) Khajenoori, M.; Rezaei, M.; Meshkani, F. Dry Reforming over $CeO_2$-promoted Ni/MgO Nano-catalyst: Effect of Ni Loading and $CH_4/CO_2$ Molar Ratio. *J. Ind. Eng. Chem.* **2015,** 21, 717-722.

(19) Choudhary, V. R.; Mamman, A. S. Energy Efficient Conversion of Methane to Syngas over NiO–MgO Solid Solution. *Appl. Energy* **2000,** 66 (2), 161-175.

(20) Min, J.-E.; Lee, Y.-J.; Park, H.-G.; Zhang, C.; Jun, K.-W. Carbon Dioxide Reforming of Methane on Ni–MgO–$Al_2O_3$ Catalysts Prepared by Sol–Gel Method: Effects of Mg/Al Ratios. *J. Ind. Eng. Chem.* **2015,** 26, 375-383.

(21) Millet, M.-M.; Tarasov, A. V.; Girgsdies, F.; Algara-Siller, G.; Schlögl, R.; Frei, E. Highly Dispersed $Ni_0/Ni_xMg_{1-x}O$ Catalysts Derived from Solid Solutions: How Metal and Support Control the $CO_2$ Hydrogenation. *ACS Catal.* **2019,** 9 (9), 8534-8546.

(22) Nagaraja, B. M.; Bulushev, D. A.; Beloshapkin, S.; Ross, J. R. H. The effect of potassium on the Activity and Stability of Ni–MgO–$ZrO_2$ Catalysts for the Dry Reforming of Methane to Give Synthesis Gas. *Catal. Today* **2011,** 178 (1), 132-136.

(23) Zhang, S.; Muratsugu, S.; Ishiguro, N.; Tada, M. Ceria-Doped Ni/SBA-16 Catalysts for Dry Reforming of Methane. *ACS Catal.* **2013,** 3 (8), 1855-1864.

(24) Damyanova, S.; Pawelec, B.; Palcheva, R.; Karakirova, Y.; Sanchez, M. C. C.; Tyuliev, G.; Gaigneaux, E.; Fierro, J. L. G. Structure and Surface Properties of Ceria-modified Ni-based Catalysts for Hydrogen Production. *Appl. Catal., B* **2018,** 225, 340-353.

(25) Estifaee, P.; Haghighi, M.; Babaluo, A. A.; Rahemi, N.; Jafari, M. F. The Beneficial Use of Non-thermal Plasma in Synthesis of $Ni/Al_2O_3$–MgO Nanocatalyst Used in Hydrogen Production from Reforming of $CH_4/CO_2$ Greenhouse Gases. *J. Power Sources* **2014,** 257, 364-373.

(26) Baktash, E.; Littlewood, P.; Schomäcker, R.; Thomas, A.; Stair, P. C. Alumina coated Nickel Nanoparticles as a Highly Active Catalyst for Dry Reforming of Methane. *Appl. Catal., B* **2015,** 179, 122-127.

(27) Abdollahifar, M.; Haghighi, M.; Babaluo, A. A.; Talkhoncheh, S. K. Sono-synthesis and Characterization of Bimetallic Ni–$Co/Al_2O_3$–MgO Nanocatalyst: Effects of Metal Content on Catalytic Properties and Activity for Hydrogen Production via $CO_2$ Reforming of $CH_4$. *Ultrason. Sonochem.* **2016,** 31, 173-183.

(28) Lovell, E. C.; Horlyck, J.; Scott, J.; Amal, R. Flame Spray Pyrolysis-designed Silica/Ceria-Zirconia Supports for the Carbon Dioxide Reforming of Methane. *Appl. Catal., A* **2017,** 546, 47-57.

(29) Koirala, R.; Pratsinis, S. E.; Baiker, A. Synthesis of Catalytic Materials in Flames: Opportunities and Challenges. *Chem. Soc. Rev.* **2016,** 45 (11), 3053-3068.

(30) Schimmoeller, B.; Pratsinis, S. E.; Baiker, A. Flame Aerosol Synthesis of Metal Oxide Catalysts with Unprecedented Structural and Catalytic Properties. *ChemCatChem* **2011,** 3 (8), 1234-1256.

(31) Horlyck, J.; Pokhrel, S.; Lovell, E.; Bedford, N. M.; Mädler, L.; Amal, R.; Scott, J. Unifying Double Flame Spray Pyrolysis with Lanthanum Doping to Restrict Cobalt–Aluminate Formation in $Co/Al_2O_3$ Catalysts for the Dry Reforming of Methane. *Catal. Sci. Technol.* **2019,** 9 (18), 4970-4980.

(32) Lovell, E. C.; Großman, H.; Horlyck, J.; Scott, J.; Mädler, L.; Amal, R. Asymmetrical Double Flame Spray Pyrolysis-Designed $SiO_2/Ce_{0.7}Zr_{0.3}O_2$ for the Dry Reforming of Methane. *ACS Appl. Mater. Interfaces* **2019,** 11 (29), 25766-25777.

(33) Mohammadi, M. M.; Gunturi, S. S.; Shao, S.; Konda, S.; Buchner, R. D.; Swihart, M. T. Flame-synthesized Nickel-Silver Nanoparticle Inks Provide High Conductivity without Sintering. *Chem. Eng. J.* **2019,** 372, 648-655.

(34) "Anderson J. E., Bool L. E.; Arnold G. W., Leger C. B., Hot Gas Atomization. US6565010B2, **2003**.

(35) Anderson, J. E.; Francis, A. W.; Wagner, M. L.; Leger, C. B., Hot Gas Reactor and Process for using Same. EP0983790A3, **2000**.

(36) Anderson, J. E., Thermal Nozzle Combustion Method. US5266024A, **1993**.

(37) Meshkani, F.; Rezaei, M. Ni Catalysts Supported on Nanocrystalline Magnesium Oxide for Syngas Production by $CO_2$ Reforming of $CH_4$. *J. Nat. Gas Chem.* **2011,** 20 (2), 198-203.

(38) Yu, M.; Zhu, K.; Liu, Z.; Xiao, H.; Deng, W.; Zhou, X. Carbon Dioxide Reforming of Methane over Promoted $Ni_xMg_{1-x}O$ (111) Platelet Catalyst Derived from Solvothermal Synthesis. *Appl. Catal., B* **2014,** 148-149, 177-190.

(39) Wurzler, G. T.; Rabelo-Neto, R. C.; Mattos, L. V.; Fraga, M. A.; Noronha, F. B. Steam Reforming of Ethanol for Hydrogen Production over MgO-supported Ni-based Catalysts. *Appl. Catal., A* **2016,** 518, 115-128.

(40) Wang, F.; Han, B.; Zhang, L.; Xu, L.; Yu, H.; Shi, W. $CO_2$ Reforming with Methane over Small-sized Ni@$SiO_2$ Catalysts with Unique Features of Sintering-free and Low Carbon. *Appl. Catal., B* **2018,** 235, 26-35.

(41) Al-Swai, B. M.; Osman, N.; Alnarabiji, M. S.; Adesina, A. A.; Abdullah, B. Syngas Production via Methane Dry Reforming over Ceria–Magnesia Mixed Oxide-Supported Nickel Catalysts. *Ind. Eng. Chem. Res.* **2019,** 58 (2), 539-552.

(42) Fang, X.; Zhang, J.; Liu, J.; Wang, C.; Huang, Q.; Xu, X.; Peng, H.; Liu, W.; Wang, X.; Zhou, W. Methane Dry Reforming over Ni/Mg-Al-O: On the Significant Promotional Effects of Rare Earth Ce and Nd Metal Oxides. *J. $CO_2$ Util.* **2018,** 25, 242-253.

(43) Fuente, S. A.; Ferretti, C. A.; Domancich, N. F.; Díez, V. K.; Apesteguía, C. R.; Di Cosimo, J. I.; Ferullo, R. M.; Castellani, N. J. Adsorption of 2-Propanol on MgO Surface: A Combined Experimental and Theoretical Study. *Appl. Surf. Sci.* **2015,** 327, 268-276.

(44) Sadeq Al-Fatesh, A.; Olajide Kasim, S.; Aidid Ibrahim, A.; Hamza Fakeeha, A.; Elhag Abasaeed, A.; Alrasheed, R.; Ashamari, R.; Bagabas, A. Combined Magnesia, Ceria and Nickel Catalyst Supported over γ-Alumina Doped with Titania for Dry Reforming of Methane. *Catalysts* **2019,** 9 (2), 188.

(45) Wang, Y.; Yao, L.; Wang, S.; Mao, D.; Hu, C. Low-temperature Catalytic $CO_2$ Dry Reforming of Methane on Ni-based Catalysts: A review. *Fuel Process. Technol.* **2018,** 169, 199-206.

(46) Pakhare, D.; Schwartz, V.; Abdelsayed, V.; Haynes, D.; Shekhawat, D.; Poston, J.; Spivey, J. Kinetic and Mechanistic Study of Dry ($CO_2$) Reforming of Methane over Rh-Substituted $La_2Zr_2O_7$ Pyrochlores. *Journal of Catalysis* **2014,** 316, 78-92.

(47) Park, J.-H.; Yeo, S.; Chang, T.-S. Effect of Supports on the Performance of Co-based Catalysts in Methane Dry Reforming. *J. $CO_2$ Util* **2018,** 26, 465-475.

(48) Zhang, L.; Wang, X.; Chen, C.; Zou, X.; Ding, W.; Lu, X. Dry Reforming of Methane to Syngas over Lanthanum-modified Mesoporous Nickel Aluminate/γ-Alumina Nanocomposites by One-pot Synthesis. *Int. J. Hydrog. Energy* **2017,** 42 (16), 11333-11345.

(49) Pino, L.; Italiano, C.; Laganà, M.; Vita, A.; Recupero, V. Kinetic Study of the Methane Dry ($CO_2$) Reforming Reaction over the $Ce_{0.70}La_{0.20}Ni_{0.10}O_{2-\delta}$ Catalyst. *Catal. Sci. Technol.* **2020,** 10 (8), 2652-2662.

(50) Nikoo, M. K.; Amin, N. A. S. Thermodynamic Analysis of Carbon Dioxide Reforming of Methane in View of Solid Carbon Formation. *Fuel Process. Technol.* **2011,** 92 (3), 678-691.

(51) Sharma, M. K.; Qi, D.; Buchner, R. D.; Scharmach, W. J.; Papavassiliou, V.; Swihart, M. T. Flame-driven Aerosol Synthesis of Copper-Nickel Nanopowders and Conductive Nanoparticle Films. *ACS Appl. Mater. Interfaces* **2014,** 6 (16), 13542-13551.

(52) Djaidja, A.; Libs, S.; Kiennemann, A.; Barama, A. Characterization and Activity in Dry Reforming of Methane on NiMg/Al and Ni/MgO Catalysts. *Catal. Today* **2006,** 113 (3), 194-200.

(53) Yan, X.; Hu, T.; Liu, P.; Li, S.; Zhao, B.; Zhang, Q.; Jiao, W.; Chen, S.; Wang, P.; Lu, J.; Fan, L.; Deng, X.; Pan, Y.-X. Highly Efficient and Stable Ni/$CeO_2$-$SiO_2$ Catalyst for Dry Reforming of Methane: Effect of Interfacial Structure of Ni/$CeO_2$ on $SiO_2$. *Appl. Catal., B* **2019,** 246, 221-231.

(54) Mohammadi, M. M.; Shao, S.; Srivatsa Gunturi, S.; Raghavan, A. R.; Alexander, N.; Liu, Y.; Stafford, C. M.; Buchner, R. D.; Swihart, M. T. A General Approach to Multicomponent Metal-decorated Crumpled Reduced Graphene Oxide Nanocomposites using a Flame-based Process. *Nanoscale* **2019,** 11 (41), 19571-19578.

(55) Scharmach, W. J.; Buchner, R. D.; Papavassiliou, V.; Pacouloute, P.; Swihart, M. T. A High-Temperature Reducing Jet Reactor for Flame-Based Metal Nanoparticle Production. *Aerosol Sci. Technol.* **2010,** 44 (12), 1083-1088.

(56) Konda, S.; Mohammadi, M. M.; Buchner, R. D.; Lin, H.; Swihart, M. T. Flame-based Synthesis and in situ Functionalization of Palladium Alloy Nanoparticles. *AIChE J.* **2018,** 64 (11), 3826-3834.

(57) Chen, J.; Carlson, B. D.; Toops, T. J.; Li, Z.; Lance, M. J.; Karakalos, S. G.; Choi, J.-S.; Kyriakidou, E. A. Methane Combustion Over Ni/$Ce_xZr_{1-x}O_2$ Catalysts: Impact of Ceria/Zirconia Ratio. *ChemCatChem* **2020,** 12 (21), 5558-5568.

(58) Chen, J.; Rohani, P.; Karakalos, S. G.; Lance, M. J.; Toops, T. J.; Swihart, M. T.; Kyriakidou, E. A. Boron-hyperdoped Silicon for the Selective Oxidative Dehydrogenation of Propane to Propylene. *Chem Commun.* **2020,** 56 (68), 9882-9885.

TOC Entry:

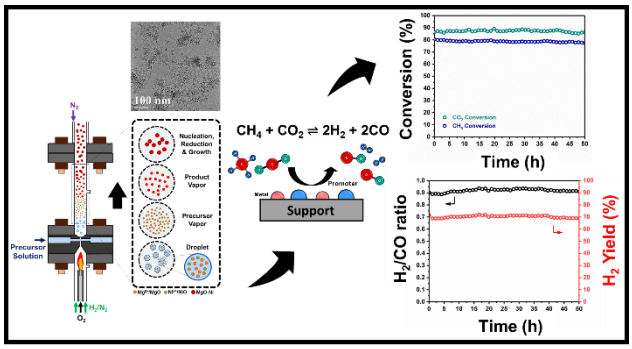
100 nm
Nucleation, Reduction & Growth
Product Vapor
Precursor Vapor
Droplet
Precursor Solution
$CH_4 + CO_2 \rightleftharpoons 2H_2 + 2CO$
Promoter
Metal
Support
Conversion (%)
Time (h)
$CO_2$ Conversion
$CH_4$ Conversion
$H_2$/CO ratio
$H_2$ Yield (%)
Time (h)